

The Mottness and the Anderson localization in bilayer nickelate $\text{La}_3\text{Ni}_2\text{O}_{7-\delta}$

Yuxin Wang,^{1,2} Ziyang Chen,^{1,2} Yi Zhang,^{3,4,*} Kun Jiang,^{1,2,†} and Jiangping Hu^{1,5,6,‡}

¹Beijing National Laboratory for Condensed Matter Physics and Institute of Physics, Chinese Academy of Sciences, Beijing 100190, China

²School of Physical Sciences, University of Chinese Academy of Sciences, Beijing 100190, China

³Department of Physics and Institute for Quantum Science and Technology, Shanghai University, Shanghai 200444, China

⁴Shanghai Key Laboratory of High Temperature Superconductors and International Center of Quantum and Molecular Structures, Shanghai University, Shanghai 200444, China

⁵Kavli Institute of Theoretical Sciences, University of Chinese Academy of Sciences, Beijing, 100190, China

⁶New Cornerstone Science Laboratory, Beijing, 100190, China

(Dated: January 16, 2025)

The oxygen content plays a pivotal role in determining the electronic properties of the recently discovered $\text{La}_3\text{Ni}_2\text{O}_{7-\delta}$ superconductors. In this work, we investigate the impact of oxygen vacancies on the insulating behavior of $\text{La}_3\text{Ni}_2\text{O}_{7-\delta}$ across the doping range $\delta = 0$ to 0.5. At $\delta = 0.5$, we construct a bilayer Hubbard model to describe the system. Using dynamical mean-field theory, we demonstrate that the model captures the characteristics of a bilayer Mott insulator. To explore the effects of disorder within the range $\delta = 0$ to 0.5, we treat the system as a mixture of metallic and Mott insulating phases. By analyzing the geometric average of the local density of states, we identify an Anderson localization transition occurring around $\delta \sim 0.2$. These results provide a quantitative explanation of recent experimental observations and highlight the critical influence of oxygen content on the physical properties of $\text{La}_3\text{Ni}_2\text{O}_{7-\delta}$.

The recent discovery of high-temperature superconductivity in bilayer nickelate $\text{La}_3\text{Ni}_2\text{O}_7$ under pressure (HP) greatly spurs the extensive research efforts in nickelate superconductors [1–6]. Many theoretical works are dedicated to understanding the origin of the high-temperature superconductivity and the corresponding pairing properties [7–21]. Additionally, many subsequent experimental studies have further enhanced our understanding and led new directions for theoretical work. For example, the angle-resolved photoemission spectroscopy (ARPES) measurements reveal the band structures of the low pressure phase [22] and a spin density wave ordered at $(\pi/2, \pi/2)$ at ambient pressure below 153K [23] is also confirmed [24–27]. These experimental findings provide physical constraints on the validity of theoretical models and approaches.

On the other hand, experimentally achieving a single phase $\text{La}_3\text{Ni}_2\text{O}_7$ is highly difficult. There are always relative structures mixing with $\text{La}_3\text{Ni}_2\text{O}_7$. A different oxygen environment leads to completely different physical properties. For example, scanning near-field optical microscopy (SNOM) experiments show nanoscale structural phase separation with different structures [28]. Therefore, it is natural to consider varying the doping level and establishing a phase diagram for nickelates to get further insight into their superconducting behavior. Interestingly, recent works showed that the superconductivity in $\text{La}_3\text{Ni}_2\text{O}_{7-\delta}$ only occurs at $\delta \leq 0.1$ (electron doping) [6, 29]. Besides, $\text{La}_3\text{Ni}_2\text{O}_{7-\delta}$ shows an insulating behavior over a wide doping range ($\delta = 0.1 - 0.5$) [29–32].

In this work, we carry out a systematic study of the $\text{La}_3\text{Ni}_2\text{O}_{7-\delta}$ within the range of $\delta = 0 \sim 0.5$, aiming to clarify the insulating behavior in this region. The main conclusions are summarized in Fig. 1 and Ref. [29]. Given that the chemical valence of O is O^{2-} , we follow the convention using electron doping $x = 2\delta$ in cuprates. The $x = 0$ phase is $\text{La}_3\text{Ni}_2\text{O}_7$, which is metallic and superconducting at high pressure. The

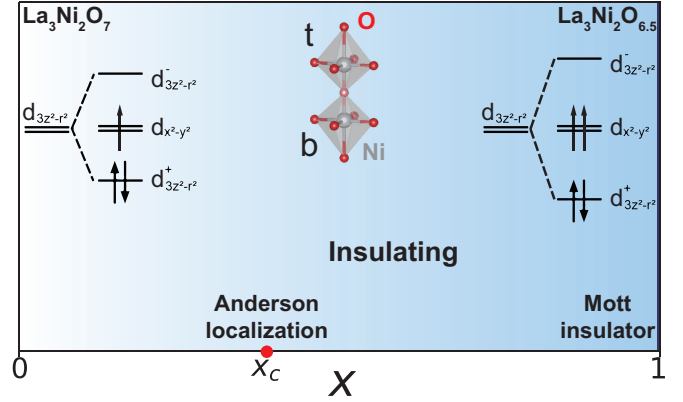


FIG. 1. The phase diagram of $\text{La}_3\text{Ni}_2\text{O}_{7-\delta}$ in the region of $\delta = 0-0.5$. The variable x represents the additional filling in the e_g orbitals of Ni introduced by the creation of O vacancies in $\text{La}_3\text{Ni}_2\text{O}_{7-\delta}$, with $x = 2\delta$ due to the chemical valence of O is O^{2-} . The crystal field splitting is also shown here and the $d_{x^2-y^2}$ orbital is exactly half-filled at $x = 1$. We also plot the enlarged bilayer Ni-O octahedral structure for large x , in which the corner shared apical pink ball can be regarded as 0.5 oxygen for $x = 1$ in VCA. The t/b indicates the layer index.

$\text{La}_3\text{Ni}_2\text{O}_{6.5}$ at $x = 1$ is a Mott insulator [29, 30, 33]. Among the doping evolution, the system becomes Anderson insulating after the critical doping x_c around 0.4.

Much like the extensively studied $\text{La}_3\text{Ni}_2\text{O}_7$, the most significant part of the crystal structure of $\text{La}_3\text{Ni}_2\text{O}_{7-\delta}$ is also the bilayer Ni-O octahedral block. However, the difference lies in the fact that the two octahedrons do not tilt even at ambient pressure for large δ , resulting in only two Ni atoms per unit cell, which we can label them as t (top layer) and b (bottom layer), as shown in the inset of Fig. 1. The crystal structure of $\delta = 0.16$ retains the orthogonal $Amam$ space group symmetry, similar to $\delta = 0$ [29]. However, for $\delta = 0.5$, the

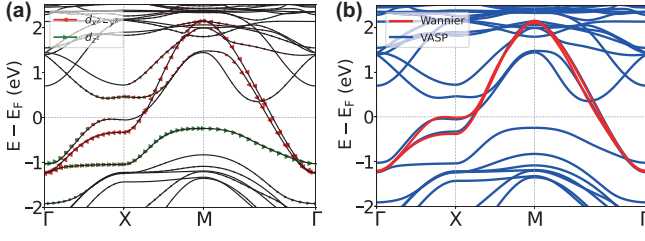


FIG. 2. (a) The band structure from DFT calculation. (b) The comparison between the first-principles calculation and wannierization. We can see the wannier bands fit the $d_{x^2-y^2}$ bands very well around the Fermi level.

tetragonal $I4/mmm$ space group is adopted, with the lattice parameters $a = 3.874\text{\AA}$ and $c = 20.075\text{\AA}$ [29]. There should be an average of 0.5 oxygen vacancies in each unit cell. Previous studies have shown that oxygen vacancies are primarily located at the corner-shared apical oxygen site between the two Ni-O octahedra (marked in pink in Fig. 1) [29, 34]. Using the virtual crystal approximation (VCA), we can model this vacancy by setting 0.5 oxygen atoms at this site in each unit cell. From this, it is evident that there are symmetry operations can map t -Ni into b -Ni, or vice versa, rendering the two Ni atoms equivalent.

The octahedron crystal field in each layer splits the five degenerate Ni $3d$ orbitals into two groups: e_g and t_{2g} . For $x = 1$, the average chemical valance of Ni is Ni^{2+} , resulting in fully occupied t_{2g} orbitals (not shown in Fig. 1) and two electrons remaining in the e_g orbitals of each Ni atom. It is important to note that the strong bilayer coupling, further splitting two d_{z^2} orbital into one bonding state $d_{z^2}^+$ and one anti-bonding state $d_{z^2}^-$, as shown in Fig. 1. However, the influence on $d_{x^2-y^2}$ orbitals can be neglected due to their geometric shape. In the bilayer block, there are a total of four electrons in the e_g orbitals, and the $d_{x^2-y^2}$ orbitals are exactly half-filled. This model is equivalent to a bilayer Hubbard model at half-filling [35–37].

We begin by considering $x = 1$ and performing first-principle density functional theory (DFT) calculations to investigate the uncorrelated electronic structure. The oxygen vacancies are treated using the VCA discussed above. Our DFT calculations are carried out with the Vienna ab-initio simulation package (VASP) code [38] with the projector augmented wave (PAW) method [39]. The generalized gradient approximation (GGA) exchange-correlation functional and its Perdew-Burke-Ernzerhof (PBE) version [40] is used. The cut-off energy for expanding the wave functions into a plane-wave basis is set to be 500 eV. The energy convergence criterion is 10^{-8} eV. All calculations are conducted using the primitive cell to save time. The Γ -centered $9 \times 9 \times 9$ k-meshes are used here. The calculated band structure is shown in Fig. 2(a). As seen, the $d_{x^2-y^2}$ bands are nearly half-filled, consistent with our previous crystal field analysis. In contrast to the GGA band structure of $x = 0$, which have been extensively studied by various research groups, the bonding d_{z^2} band here is fully occupied and inactive at Fermi level [41]. Additionally, the

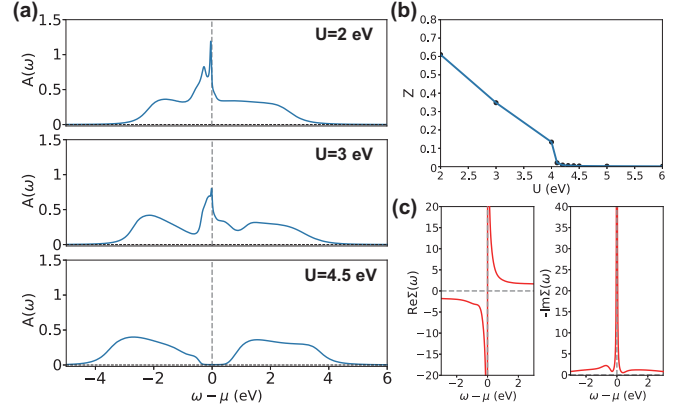


FIG. 3. (a) The spectral functions $A(\omega)$ for $x = 1$ obtained from DMFT calculation are shown for $U = 2$ eV, $U = 3$ eV and $U = 4.5$ eV, respectively. The spectral evolves from the slightly modified non-interacting density of states to a three-peak structure, and ultimately to a clear Mott gap as the correlated strength U increases. (b) The quasi-particle weight Z at the Fermi level. The Mott transition occurs around $U = 4.5$ eV. (c) The real ($\text{Re}\Sigma(\omega)$) and the negative imaginary parts ($-\text{Im}\Sigma(\omega)$) of the electronic self-energy at $U = 4.5$ eV. Both of them exhibit the standard Mott insulating behavior.

interlayer coupling is stronger at $x = 1$ for the d_{z^2} orbital, resulting in the anti-bonding d_{z^2} band being located at a higher energy than $x = 0$ and thus not appearing in Fig. 2(a).

Based on the above discussions, we can safely ignore the d_{z^2} orbitals and focus solely on the $d_{x^2-y^2}$ orbitals. The Wannier90 code [42, 43] is used to fit the $d_{x^2-y^2}$ bands obtained from previous DFT calculations. Since there are 2 atoms per unit cell, we derive a 2-band model. The dispersion of these wannierized bands is compared to the DFT bands in Fig. 2(b). As shown, the wannierized bands match the DFT bands very well around the Fermi level. Furthermore, we can extract the hopping parameters of this 2-band model. The corresponding Hamiltonian and the explicit parameters can be found in SM, which provides a faithful description of the low-energy electronic structure.

The DFT band structure for $x = 1$ clearly shows a metallic behavior, contradicting to the experimental findings [29, 30]. Therefore, it is necessary to include the correlation effect. For this bilayer single-orbital model, we consider the Hubbard interaction:

$$H_I = U \sum_{l,i} \hat{n}_{l,i\uparrow} \hat{n}_{l,i\downarrow}, \quad (1)$$

with the $l = t, b$ denoting the layer index and i the site index. To obtain the correlated band structure for $x = 1$, we perform the dynamical mean field theory (DMFT) calculations on the previously obtained Wannier90 results, adding this Hubbard interaction H_I . Our DMFT calculation is implemented using the open-source TRIQS package [44] with the continuous-time quantum Monte Carlo (CT-QMC) impurity solver CTHYB [45]. The analytical continuation is performed using the maximum entropy method implemented in Maxent

package [46]. To determine the Mott transition point, we carry out DMFT calculations for various values of U within the range of 2 eV to 6 eV. A criterion for identifying this transition point is that the quasi-particle weight Z at the Fermi level approaches to zero. It is defined as

$$Z = \left[1 - \frac{\partial \text{Re}\Sigma(\omega)}{\partial \omega} \Big|_{\omega=0} \right]^{-1}, \quad (2)$$

where $\text{Re}\Sigma(\omega)$ is the real part of the electronic self-energy at real frequency. The dependence of Z on U is shown in Fig. 3(b). It is clear that Z drops to zero at approximately $U = 4.5$ eV. Therefore, we identify the Mott transition at this U value.

To further confirm this, the spectral functions $A(\omega)$ at $U = 2$ eV, $U = 3$ eV and $U = 4.5$ eV are also plotted in Fig. 3(a). We define the W as the bandwidth, which is approximately 3 eV in this material (See Fig. 3(b)). At $U = 2$ eV, the interaction is weak compared to the kinetic energy, and $A(\omega)$ can be regarded as the slightly modified non-interacting density of states. At $U = 3$ eV, the interaction enters the intermediate regime with $U \approx W$. Thus, $A(\omega)$ should exhibit features from both the non-interacting limit $U \ll W$ and the atomic limit $U \gg W$. As a result, the characteristic three-peak structure commonly observed in strongly correlated materials emerges. As U increases, the spectral weight gradually transfers from the central quasi-particle peak to the Hubbard bands on both sides. At the critical value of $U = 4.5$ eV, the spectral clearly exhibits a Mott gap, and the corresponding electronic self-energy is displayed in Fig. 3(c). Both the real and imaginary parts demonstrate the typical behavior of a Mott insulator. The real part is distributed in the first and third quadrants, causing each band in the non-interacting band structure to split into two branches. Moreover, $\partial \text{Re}\Sigma(\omega)/\partial \omega|_{\omega=0} \rightarrow -\infty$, which is consistent with $Z = 0$. The negative imaginary part approaches $+\infty$ at $\omega = 0$, which also indicates that the $A(\omega)$ should tend to zero at this point.

Hence, the Mott transition is identified for $x = 1$ from the DMFT calculation. Importantly, the Mott insulator found here belongs to the spin singlet state, which is consistent with the experiment magnetic susceptibility measurement [30]. Our result is also consistent with the phase diagram findings of the bilayer single orbital Hubbard model in the non-magnetic case [35–37]. On the other hand, previous DFT+ U study [33] suggests that the band structure is insulating into an antiferromagnetic (AFM) state, which deviates from our results and experimental findings.

Before further discussion, we would like to emphasize that we employ the VCA approximation to construct our effective two-band model. While the VCA $\text{La}_3\text{Ni}_2\text{O}_{6.5}$ is not, strictly speaking, a realistic structure, its electronic properties are expected to closely approximate those of a more realistic system. X-ray diffraction results indicate that the symmetry group of $\text{La}_3\text{Ni}_2\text{O}_{6.5}$ aligns with $I4/mmm$, suggesting that oxygen vacancies are mostly likely randomly distributed [29, 30]. When considering the random distribution of oxygen vacancies, $\text{La}_3\text{Ni}_2\text{O}_{6.5}$ is likely to exhibit stronger insulating

behavior. Consequently, our approach remains valid within this context.

Next, we want to address the Anderson transition from $\text{La}_3\text{Ni}_2\text{O}_7$ to $\text{La}_3\text{Ni}_2\text{O}_{6.5}$. The strong correlation in $\text{La}_3\text{Ni}_2\text{O}_{6.5}$ makes the disorder effect hard for simulation. On the other hand, it is widely known that the bilayer Mott insulator smoothly connects with a bilayer band insulator [35–37]. Hence, we apply the strategy of using a bilayer band insulator to mimic the bilayer Mott effect. It turns out this is one efficient way to this Anderson localization problem.

Specifically, we treat the system as a mixture of the metallic state at $x = 0$ and the Mott insulator state at $x = 1$ to study the disorder effect due to the randomly distributed oxygen vacancies. Therefore, the Hamiltonian for this disordered system can be expressed as $H = H_0 + H_{dis}$, where H_0 is the bilayer two-orbital tight-binding model describing the metallic state at $x = 0$, which has been well studied in Ref. [41]. H_{dis} describes the disorder effect and can be expressed as

$$H_{dis} = \sum_{ij} \sum_{\alpha\beta} V_{ij,\alpha\beta} c_{i\alpha}^\dagger c_{j\beta} \quad (3)$$

where i, j are the indices of the unit cell and α, β are the combinations of the layer and orbital indices. Here $V_{ij,\alpha\beta} = V_{ij,\alpha\beta}^{Mott}$ only when unit cells i or j are affected by the oxygen vacancy and become locally Mott-localized and vanishes otherwise. $V_{ij,\alpha\beta}^{Mott}$ is determined by letting the Hamiltonian $H_{Mott} = H_0 + \sum_{ij} \sum_{\alpha\beta} V_{ij,\alpha\beta}^{Mott} c_{i\alpha}^\dagger c_{j\beta}$ describe the gapped band structure of the Mott insulator at $x = 1$. Then the real space Hamiltonian of the disordered system can be generated by considering each unit cell affected by the oxygen vacancy with the probability x_{Mott} , so that the effective oxygen vacancy becomes $\delta_{eff} = 0.5x_{Mott}$, which leads to the effective doping $x_{eff} = x_{Mott}$.

As we discussed above, this Mott insulator is driven by the correlation effect in the bilayer $d_{x^2-y^2}$ orbital and the bonding (antibonding) d_{z^2} orbital is fully occupied (unoccupied). Then, the effective bilayer model is constructed by increasing t_{\perp}^x and t_{\perp}^z . The details for this model can be found in the SM. The total density of states (DOS) and the orbital projected DOS are plotted in Fig. 4(a). The d_{z^2} bands are well separated from the $d_{x^2-y^2}$. and the $d_{x^2-y^2}$ bands are also split into two bands with gap of 1.3 eV, which is used to mimic the Mott gap for $x = 1$.

The disorder-induced localization effect can be captured by comparing the average density of states (ADOS) and the typical density of states (TDOS) defined as the arithmetic and geometric average of the local density of states (LDOS), respectively. They can be expressed as

$$\text{ADOS}(E) = \langle \rho_i(E) \rangle \quad (4)$$

$$\text{TDOS}(E) = e^{\langle \ln \rho_i(E) \rangle} \quad (5)$$

where $\rho_i(E)$ is the total LDOS for each unit cell i and $\langle \dots \rangle$ corresponds to the average over different realizations of disorder and unit cell i . This is because the probability distributions of the LDOS for a weakly disordered metal and the strongly

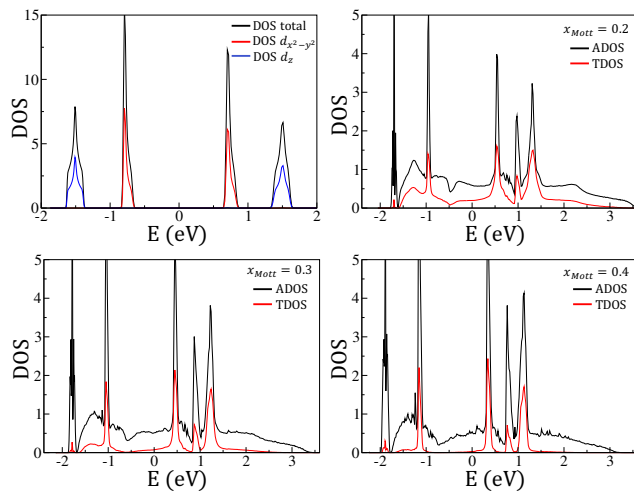


FIG. 4. (a) The density of states of the band insulator used to simulate the Mott insulator where the total DOS is the sum of both layers, while the DOS of the two orbitals are for each layer. (b) Comparison of ADOS and TDOS calculated with KPM with various doping $x = 0.2, 0.3, 0.4$. The KPM uses 1024 moments on a square lattice with size 100^2 and 256 independent disordered realizations generated with 32 sites randomly sampled from each realization. The Fermi level is shifted to zero in all plots according to the doping induced by x_{Mott} .

disordered Anderson insulator are very different. The distribution is Gaussian-like for the former and highly skewed as the log-normal distribution for the latter, where the TDOS approaches zero which can serve as an order parameter for the Anderson localization transition [47, 48]. This approach is successfully applied to the single-band Anderson model [47–50] and the realistic systems [51, 52] to study the localization effect. We thus calculate the ADOS and TDOS using the kernel polynomial method (KPM) [49, 53, 54], where the LDOS is expanded by a series of Chebyshev polynomials whose arithmetic and geometric average can then be evaluated as the ADOS and TDOS. The Jackson kernel is used in the KPM calculations [49].

The calculated ADOS and TDOS are shown in Figs. 4(b-d) for three values of x_{Mott} . In the calculation, the Fermi level is determined by matching the integrated ADOS up to the Fermi level with the corresponding effective doping levels, which is shifted to zero in all the plots. When $x_{Mott} = 0.2$, both ADOS and TDOS are finite at the Fermi level, which means the states around the Fermi level are still delocalized and the system is still metallic. However, as x_{Mott} increases, i.e. the oxygen vacancies increase, the TDOS at the Fermi level starts to decrease and approaches zero at $x_{Mott} = 0.4$ while the ADOS remains finite at all values of x_{Mott} . This indicates that the states at the Fermi level become more and more localized as x_{Mott} increases and the system becomes an insulator around the critical value at $x_c = 0.4$ ($\delta_c = 0.2$), where the TDOS at the Fermi level vanishes, signaling the Anderson localization transition, which is consistent with the experimental observations [29].

In summary, we perform a theoretical investigation on the $\text{La}_3\text{Ni}_2\text{O}_{7-\delta}$ within the range of $\delta = 0 \sim 0.5$. For the $\delta = 0.5$ phase, the low energy physics of $\text{La}_3\text{Ni}_2\text{O}_{6.5}$ is dominated by the bilayer $d_{x^2-y^2}$ orbital. Further considering the electron correlation effect in this bilayer model, a bilayer Mott insulator phase is identified through the DMFT calculation. This result matches well with recent experimental findings [29, 30]. Furthermore, we consider the doping transition from $x = 0$ to $x = 1$ through mixing the metallic $\text{La}_3\text{Ni}_2\text{O}_7$ and insulating $\text{La}_3\text{Ni}_2\text{O}_{6.5}$. By evaluating the ADOS and TDOS at the Fermi level, we identify an Anderson localization transition driven by randomly distributed oxygen vacancies. This transition occurs at a critical doping of $x_c = 0.4$ ($\delta_c = 0.2$), in good agreement with recent experimental findings [29].

More importantly, we notice that the $\text{La}_3\text{Ni}_2\text{O}_{7-\delta}$ thin film has been successfully synthesized [55–57]. However, besides the compressive stress effects, the $\text{La}_3\text{Ni}_2\text{O}_{7-\delta}$ thin films always show insulating features at low-temperature [55–57]. Based on this work, we want to point out that the deficiency of oxygen content in these thin films may be one key reason for realizing the metallic phase and the superconducting phase [56, 57]. We hope our findings can provide a new perspective for insulating behaviors in $\text{La}_3\text{Ni}_2\text{O}_{7-\delta}$.

Acknowledgement: We acknowledge the support by the National Natural Science Foundation of China (Grant NSFC-12494594, No. NSFC-11888101, No. NSFC-12174428, and No. NSFC-12274279), the Ministry of Science and Technology (Grant No. 2022YFA1403900), the New Cornerstone Investigator Program, and the Chinese Academy of Sciences Project for Young Scientists in Basic Research (2022YSBR-048).

* zhangyi821@shu.edu.cn

† jiangkun@iphy.ac.cn

‡ jphu@iphy.ac.cn

- [1] Hualei Sun, Mengwu Huo, Xunwu Hu, Jingyuan Li, Zengjia Liu, Yifeng Han, Lingyun Tang, Zhongquan Mao, Pengtao Yang, Bosen Wang, Jinguang Cheng, Dao-Xin Yao, Guang-Ming Zhang, and Meng Wang, “Signatures of superconductivity near 80 K in a nickelate under high pressure,” *Nature* **621**, 493–498 (2023).
- [2] Gang Wang, Ningning Wang, Yuxin Wang, Lifen Shi, Xiaoling Shen, Jun Hou, Hanming Ma, Pengtao Yang, Ziyi Liu, Hua Zhang, Xiaoli Dong, Jianping Sun, Bosen Wang, Kun Jiang, Jiangping Hu, Yoshiya Uwatoko, and Jinguang Cheng, “Observation of high-temperature superconductivity in the high-pressure tetragonal phase of $\text{La}_2\text{PrNi}_2\text{O}_{7-\delta}$,” *arXiv e-prints*, arXiv:2311.08212 (2023).
- [3] Jun Hou, Peng-Tao Yang, Zi-Yi Liu, Jing-Yuan Li, Peng-Fei Shan, Liang Ma, Gang Wang, Ning-Ning Wang, Hai-Zhong Guo, Jian-Ping Sun, *et al.*, “Emergence of high-temperature superconducting phase in pressurized $\text{La}_3\text{Ni}_2\text{O}_7$ crystals,” *Chinese Physics Letters* **40**, 117302 (2023).
- [4] Yanan Zhang, Dajun Su, Yanen Huang, Hualei Sun, Mengwu Huo, Zhaoyang Shan, Kaixin Ye, Zihan Yang, Rui Li, Michael Smidman, Meng Wang, Lin Jiao, and Huiqiu Yuan, “High-

- temperature superconductivity with zero resistance and strange-metal behaviour in $\text{La}_3\text{Ni}_2\text{O}_{7-\delta}$,” *Nature Physics*, 1–5 (2024).
- [5] G. Wang, N. N. Wang, X. L. Shen, J. Hou, L. Ma, L. F. Shi, Z. A. Ren, Y. D. Gu, H. M. Ma, P. T. Yang, Z. Y. Liu, H. Z. Guo, J. P. Sun, G. M. Zhang, S. Calder, J.-Q. Yan, B. S. Wang, Y. Uwatoko, and J.-G. Cheng, “Pressure-Induced Superconductivity In Polycrystalline $\text{La}_3\text{Ni}_2\text{O}_{7-\delta}$,” *Phys. Rev. X* **14**, 011040 (2024).
- [6] Yazhou Zhou, Jing Guo, Shu Cai, Hualei Sun, Pengyu Wang, Jinyu Zhao, Jinyu Han, Xintian Chen, Qi Wu, Yang Ding, Meng Wang, Tao Xiang, Ho-kwang Mao, and Liling Sun, “Evidence of filamentary superconductivity in pressurized $\text{La}_3\text{Ni}_2\text{O}_7$ single crystals,” [arXiv preprint arXiv:2311.12361](https://arxiv.org/abs/2311.12361).
- [7] Zhihui Luo, Xunwu Hu, Meng Wang, Wéi Wú, and Dao-Xin Yao, “Bilayer Two-Orbital Model of $\text{La}_3\text{Ni}_2\text{O}_7$ under Pressure,” *Phys. Rev. Lett.* **131**, 126001 (2023).
- [8] Yang Zhang, Ling-Fang Lin, Adriana Moreo, and Elbio Dagotto, “Electronic structure, dimer physics, orbital-selective behavior, and magnetic tendencies in the bilayer nickelate superconductor $\text{La}_3\text{Ni}_2\text{O}_7$ under pressure,” *Phys. Rev. B* **108**, L180510 (2023).
- [9] Qing-Geng Yang, Da Wang, and Qiang-Hua Wang, “Possible s_{\pm} -wave superconductivity in $\text{La}_3\text{Ni}_2\text{O}_7$,” *Phys. Rev. B* **108**, L140505 (2023).
- [10] Hirofumi Sakakibara, Naoya Kitamine, Masayuki Ochi, and Kazuhiko Kuroki, “Possible High T_c Superconductivity in $\text{La}_3\text{Ni}_2\text{O}_7$ under High Pressure through Manifestation of a Nearly Half-Filled Bilayer Hubbard Model,” *Phys. Rev. Lett.* **132**, 106002 (2024).
- [11] Yuhao Gu, Congcong Le, Zhesen Yang, Xianxin Wu, and Jiangping Hu, “Effective model and pairing tendency in bilayer Ni-based superconductor $\text{La}_3\text{Ni}_2\text{O}_7$,” [arXiv e-prints](https://arxiv.org/abs/2306.07275), [arXiv:2306.07275](https://arxiv.org/abs/2306.07275) (2023).
- [12] Shen Yang *et al.*, “Effective Bi-Layer Model Hamiltonian and Density-Matrix Renormalization Group Study for the High- T_c Superconductivity in $\text{La}_3\text{Ni}_2\text{O}_7$ under High Pressure,” *Chinese Physics Letters* **40**, 127401 (2023).
- [13] Viktor Christiansson, Francesco Petocchi, and Philipp Werner, “Correlated Electronic Structure of $\text{La}_3\text{Ni}_2\text{O}_7$ under Pressure,” *Phys. Rev. Lett.* **131**, 206501 (2023).
- [14] Yu-Bo Liu, Jia-Wei Mei, Fei Ye, Wei-Qiang Chen, and Fan Yang, “ s^{\pm} -Wave Pairing and the Destructive Role of Apical-Oxygen Deficiencies in $\text{La}_3\text{Ni}_2\text{O}_7$ under Pressure,” *Phys. Rev. Lett.* **131**, 236002 (2023).
- [15] Chen Lu, Zhiming Pan, Fan Yang, and Congjun Wu, “Interlayer-Coupling-Driven High-Temperature Superconductivity in $\text{La}_3\text{Ni}_2\text{O}_7$ under Pressure,” *Phys. Rev. Lett.* **132**, 146002 (2024).
- [16] Yang Zhang, Ling-Fang Lin, Adriana Moreo, Thomas A Maier, and Elbio Dagotto, “Structural phase transition, s_{\pm} -wave pairing, and magnetic stripe order in bilayered superconductor $\text{La}_3\text{Ni}_2\text{O}_7$ under pressure,” *Nature Communications* **15**, 2470 (2024).
- [17] Yi-feng Yang, Guang-Ming Zhang, and Fu-Chun Zhang, “Interlayer valence bonds and two-component theory for high- T_c superconductivity of $\text{La}_3\text{Ni}_2\text{O}_7$ under pressure,” *Phys. Rev. B* **108**, L201108 (2023).
- [18] Siheon Ryee, Niklas Witt, and Tim O Wehling, “Critical role of interlayer dimer correlations in the superconductivity of $\text{La}_3\text{Ni}_2\text{O}_7$,” [arXiv preprint](https://arxiv.org/abs/2310.17465), [arXiv:2310.17465](https://arxiv.org/abs/2310.17465) (2023).
- [19] Kun Jiang, Ziqiang Wang, and Fu-Chun Zhang, “High-temperature superconductivity in $\text{La}_3\text{Ni}_2\text{O}_7$,” *Chinese Physics Letters* **41**, 017402 (2024).
- [20] Frank Lechermann, Jannik Gondolf, Steffen Bötzel, and Ilya M. Eremin, “Electronic correlations and superconducting instability in $\text{La}_3\text{Ni}_2\text{O}_7$ under high pressure,” *Phys. Rev. B* **108**, L201121 (2023).
- [21] Zhenfeng Ouyang, Jia-Ming Wang, Jing-Xuan Wang, Rong-Qiang He, Li Huang, and Zhong-Yi Lu, “Hund electronic correlation in $\text{La}_3\text{Ni}_2\text{O}_7$ under high pressure,” *Phys. Rev. B* **109**, 115114 (2024).
- [22] Jiangang Yang, Hualei Sun, Xunwu Hu, Yuyang Xie, Taimin Miao, Hailan Luo, Hao Chen, Bo Liang, Wenpei Zhu, Gexing Qu, *et al.*, “Orbital-dependent electron correlation in double-layer nickelate $\text{La}_3\text{Ni}_2\text{O}_7$,” *Nature Communications* **15**, 4373 (2024).
- [23] Zengjia Liu, Hualei Sun, Mengwu Huo, Xiaoyan Ma, Yi Ji, Enkui Yi, Lisi Li, Hui Liu, Jia Yu, Ziyou Zhang, Zhiqiang Chen, Feixiang Liang, Hongliang Dong, Hanjie Guo, Dingyong Zhong, Bing Shen, Shiliang Li, and Meng Wang, “Evidence for charge and spin density waves in single crystals of $\text{La}_3\text{Ni}_2\text{O}_7$ and $\text{La}_3\text{Ni}_2\text{O}_6$,” *Science China Physics, Mechanics & Astronomy* **66**, 217411 (2022).
- [24] Xiaoyang Chen, Jaewon Choi, Zhicheng Jiang, Jiong Mei, Kun Jiang, Jie Li, Stefano Agrestini, Mirian Garcia-Fernandez, Xing Huang, Hualei Sun, Dawei Shen, Meng Wang, Jiangping Hu, Yi Lu, Ke-Jin Zhou, and Donglai Feng, “Electronic and magnetic excitations in $\text{La}_3\text{Ni}_2\text{O}_7$,” [arXiv e-prints](https://arxiv.org/abs/2401.12657), [arXiv:2401.12657](https://arxiv.org/abs/2401.12657) (2024).
- [25] Zhao Dan, Yanbing Zhou, Mengwu Huo, Yu Wang, Linpeng Nie, Meng Wang, Tao Wu, and Xianhui Chen, “Spin-density-wave transition in double-layer nickelate $\text{La}_3\text{Ni}_2\text{O}_7$,” [arXiv e-prints](https://arxiv.org/abs/2402.03952), [arXiv:2402.03952](https://arxiv.org/abs/2402.03952) (2024).
- [26] Kaiwen Chen, Xiangqi Liu, Jiachen Jiao, Muyuan Zou, Chengyu Jiang, Xin Li, Yixuan Luo, Qiong Wu, Ningyuan Zhang, Yanfeng Guo, and Lei Shu, “Evidence of Spin Density Waves in $\text{La}_3\text{Ni}_2\text{O}_{7-\delta}$,” *Phys. Rev. Lett.* **132**, 256503 (2024).
- [27] Rustem Khasanov, Thomas J. Hicken, Dariusz J. Gawryluk, Loïc Pierre Sorel, Steffen Bötzel, Frank Lechermann, Ilya M. Eremin, Hubertus Luetkens, and Zurab Guguchia, “Pressure-Induced Split of the Density Wave Transitions in $\text{La}_3\text{Ni}_2\text{O}_{7-\delta}$,” [arXiv e-prints](https://arxiv.org/abs/2402.10485) (2024), [arXiv:2402.10485](https://arxiv.org/abs/2402.10485).
- [28] Xiaoxiang Zhou, Weihong He, Zijian Zhou, Kaipeng Ni, Mengwu Huo, Deyuan Hu, Yinghao Zhu, Enkang Zhang, Zhicheng Jiang, Shuaikang Zhang, *et al.*, “Revealing nanoscale structural phase separation in $\text{La}_3\text{Ni}_2\text{O}_{7-\delta}$ single crystal via scanning near-field optical microscopy,” [arXiv preprint](https://arxiv.org/abs/2410.06602) [arXiv:2410.06602](https://arxiv.org/abs/2410.06602) (2024).
- [29] Yuta Ueki, Hiroya Sakurai, Hibiki Nagata, Kazuki Yamane, Ryo Matsumoto, Kensei Terashima, Keisuke Hirose, Hiroto Ohta, Masaki Kato, and Yoshihiko Takano, “Phase diagram of pressure-induced high temperature superconductor $\text{La}_3\text{Ni}_2\text{O}_{7+\delta}$,” [arXiv preprint](https://arxiv.org/abs/2408.04970) [arXiv:2408.04970](https://arxiv.org/abs/2408.04970) (2024).
- [30] Ran Gao, Lun Jin, Shuyuan Huyan, Danrui Ni, Haozhe Wang, Xianghan Xu, Sergey L. Bud’ko, Paul Canfield, Weiwei Xie, and Robert J. Cava, “Is $\text{La}_3\text{Ni}_2\text{O}_{6.5}$ a Bulk Superconducting Nickelate?” *ACS Applied Materials & Interfaces*, *ACS Applied Materials & Interfaces* (2024), 10.1021/acsami.3c17376.
- [31] Z. Zhang, M. Greenblatt, and J.B. Goodenough, “Synthesis, Structure, and Properties of the Layered Perovskite $\text{La}_3\text{Ni}_2\text{O}_{7-\delta}$,” *Journal of Solid State Chemistry* **108**, 402–409 (1994).
- [32] Viktor V. Poltavets, Konstantin A. Lokshin, Takeshi Egami, and Martha Greenblatt, “The oxygen deficient Ruddlesden–Popper $\text{La}_3\text{Ni}_2\text{O}_{7-\delta}$ ($\delta=0.65$) phase: Structure and properties,” *Materials Research Bulletin* **41**, 955–960 (2006), special Issue Dedicated to Prof. Gerard Ferey.
- [33] Victor Pardo and Warren E. Pickett, “Metal-insulator transition

- in layered nickelates $\text{La}_3\text{Ni}_2\text{O}_{7-\delta}$ ($\delta = 0.0, 0.5, 1$),” *Phys. Rev. B* **83**, 245128 (2011).
- [34] Zehao Dong, Mengwu Huo, Jie Li, Jingyuan Li, Pengcheng Li, Hualei Sun, Lin Gu, Yi Lu, Meng Wang, Yayu Wang, *et al.*, “Visualization of oxygen vacancies and self-doped ligand holes in $\text{La}_3\text{Ni}_2\text{O}_{7-\delta}$,” *Nature*, 1–6 (2024).
- [35] Andreas Fuhrmann, David Heilmann, and Hartmut Monien, “From mott insulator to band insulator: A dynamical mean-field theory study,” *Phys. Rev. B* **73**, 245118 (2006).
- [36] S. S. Kancharla and S. Okamoto, “Band insulator to mott insulator transition in a bilayer hubbard model,” *Phys. Rev. B* **75**, 193103 (2007).
- [37] Yi Zhang, Yuhao Gu, Hongming Weng, Kun Jiang, and Jiangping Hu, “Mottness in two-dimensional van der Waals Nb_3X_8 monolayers ($X = \text{Cl}, \text{Br}, \text{and I}$),” *Phys. Rev. B* **107**, 035126 (2023).
- [38] G. Kresse and J. Furthmüller, “Efficient iterative schemes for ab initio total-energy calculations using a plane-wave basis set,” *Phys. Rev. B* **54**, 11169–11186 (1996).
- [39] G. Kresse and D. Joubert, “From ultrasoft pseudopotentials to the projector augmented-wave method,” *Phys. Rev. B* **59**, 1758–1775 (1999).
- [40] John P. Perdew, Kieron Burke, and Matthias Ernzerhof, “Generalized gradient approximation made simple,” *Phys. Rev. Lett.* **77**, 3865–3868 (1996).
- [41] Yuxin Wang, Kun Jiang, Ziqiang Wang, Fu-Chun Zhang, and Jiangping Hu, “Electronic and magnetic structures of bilayer $\text{La}_3\text{Ni}_2\text{O}_7$ at ambient pressure,” *Phys. Rev. B* **110**, 205122 (2024).
- [42] Arash A Mostofi, Jonathan R Yates, Young-Su Lee, Ivo Souza, David Vanderbilt, and Nicola Marzari, “wannier90: A tool for obtaining maximally-localised Wannier functions,” *Computer physics communications* **178**, 685–699 (2008).
- [43] Nicola Marzari, Arash A. Mostofi, Jonathan R. Yates, Ivo Souza, and David Vanderbilt, “Maximally localized wannier functions: Theory and applications,” *Rev. Mod. Phys.* **84**, 1419–1475 (2012).
- [44] Olivier Parcollet, Michel Ferrero, Thomas Ayrál, Hartmut Hafermann, Igor Krivenko, Laura Messio, and Priyanka Seth, “TRIQS: A toolbox for research on interacting quantum systems,” *Computer Physics Communications* **196**, 398 – 415 (2015).
- [45] Priyanka Seth, Igor Krivenko, Michel Ferrero, and Olivier Parcollet, “TRIQS/CTHYB: A continuous-time quantum Monte Carlo hybridisation expansion solver for quantum impurity problems,” *Computer Physics Communications* **200**, 274 – 284 (2016).
- [46] Gernot J. Kraberger, Robert Triebl, Manuel Zingl, and Markus Aichhorn, “Maximum entropy formalism for the analytic continuation of matrix-valued Green’s functions,” *Phys. Rev. B* **96**, 155128 (2017).
- [47] V. Dobrosavljević, A. A. Pastor, and B. K. Nikolić, “Typical medium theory of anderson localization: A local order parameter approach to strong-disorder effects,” *Europhysics Letters* **62**, 76 (2003).
- [48] Gerald Schubert, Jens Schleede, Krzysztof Byczuk, Holger Fehske, and Dieter Vollhardt, “Distribution of the local density of states as a criterion for anderson localization: Numerically exact results for various lattices in two and three dimensions,” *Phys. Rev. B* **81**, 155106 (2010).
- [49] Alexander Weiße, Gerhard Wellein, Andreas Alvermann, and Holger Fehske, “The kernel polynomial method,” *Rev. Mod. Phys.* **78**, 275–306 (2006).
- [50] C. E. Ekuma, H. Terletska, K.-M. Tam, Z.-Y. Meng, J. Moreno, and M. Jarrell, “Typical medium dynamical cluster approximation for the study of anderson localization in three dimensions,” *Phys. Rev. B* **89**, 081107 (2014).
- [51] Yi Zhang, Hanna Terletska, C. Moore, Chinedu Ekuma, Ka-Ming Tam, Tom Berlijn, Wei Ku, Juana Moreno, and Mark Jarrell, “Study of multiband disordered systems using the typical medium dynamical cluster approximation,” *Phys. Rev. B* **92**, 205111 (2015).
- [52] Yi Zhang, R. Nelson, Elisha Siddiqui, K.-M. Tam, U. Yu, T. Berlijn, W. Ku, N. S. Vidhyadhiraja, J. Moreno, and M. Jarrell, “Generalized multiband typical medium dynamical cluster approximation: Application to $(\text{Ga},\text{Mn})\text{N}$,” *Phys. Rev. B* **94**, 224208 (2016).
- [53] Gerald Schubert, Alexander Weiße, and Holger Fehske, “Localization effects in quantum percolation,” *Phys. Rev. B* **71**, 045126 (2005).
- [54] Gerald Schubert and Holger Fehske, “Dynamical aspects of two-dimensional quantum percolation,” *Phys. Rev. B* **77**, 245130 (2008).
- [55] Ting Cui, Songhee Choi, Ting Lin, Chen Liu, Gang Wang, Ningning Wang, Shengru Chen, Haitao Hong, Dongke Rong, Qianying Wang, Qiao Jin, Jia-Ou Wang, Lin Gu, Chen Ge, Can Wang, Jin-Guang Cheng, Qinghua Zhang, Liang Si, Kuijuan Jin, and Er-Jia Guo, “Strain-mediated phase crossover in ruddlesden–popper nickelates,” *Communications Materials* **5**, 32 (2024).
- [56] Eun Kyo Ko, Yijun Yu, Yidi Liu, Lopa Bhatt, Jiarui Li, Vivek Thampy, Cheng-Tai Kuo, Bai Yang Wang, Yonghun Lee, Kyuho Lee, Jun-Sik Lee, Berit H. Goodge, David A. Muller, and Harold Y. Hwang, “Signatures of ambient pressure superconductivity in thin film $\text{La}_3\text{Ni}_2\text{O}_7$,” *Nature* (2024), 10.1038/s41586-024-08525-3.
- [57] Guangdi Zhou, Wei Lv, Heng Wang, Zihao Nie, Yaqi Chen, Yueying Li, Haoliang Huang, Weiqiang Chen, Yujie Sun, Qikun Xue, and Zhuoyu Chen, “Ambient-pressure superconductivity onset above 40 K in bilayer nickelate ultrathin films,” (2024), arXiv:2412.16622 [cond-mat.supr-con].

Supplemental Materials: The Mottness and the Anderson localization in bilayer nickelate $\text{La}_3\text{Ni}_2\text{O}_{7-\delta}$

t_1^x	t_2^x	t_3^x	t_\perp^x	$t_{\perp 1}^x$	$t_{\perp 2}^x$	$t_{\perp 3}^x$	ϵ^x
-0.3902	0.0837	-0.0333	0.0224	0.0089	-0.0228	0.0219	0.2509

TABLE S1. The hopping parameters of the TB Hamiltonian $H(\mathbf{k})$ obtained from Wannier90 in unit of eV. ϵ^x is site energies for Ni $d_{x^2-y^2}$ orbital.

t_1^x	t_1^z	t_2^x	t_2^z	t_3^{xz}
-0.6003	-0.149	0.0391	-0.0007	0.2679
t_\perp^x	t_\perp^z	t_4^{xz}	ϵ^x	ϵ^z
0.038	-0.999	-0.072	1.2193	0.0048

t_1^x	t_1^z	t_2^x	t_2^z	t_3^{xz}
-0.0153	-0.0298	0.00782	-0.00014	0.01
t_\perp^x	t_\perp^z	t_4^{xz}	ϵ^x	ϵ^z
-0.75	-1.4985	-0.0144	-0.148	-0.1408

TABLE S2. The hopping parameters of the TB Hamiltonian used for the Anderson transition calculations. The upper panel corresponds to the bilayer two-orbital model H_0 describing the metallic state at $x = 0$ [41]. The lower panel corresponds to H_{Mott} used to describe the gapped band structure of the Mott insulator state at $x = 1$. All parameters are in the unit of eV.

THE TIGHT-BINDING MODEL FOR $\text{La}_3\text{Ni}_2\text{O}_{6.5}$

Here, we list the 2-band TB model used in the Mott transition calculations mentioned in the main text. Based on the discussion in the main text, our TB model considers only the $d_{x^2-y^2}$ orbital on each Ni site. On a square lattice, the TB model can be written as:

$$H_{TB}(\mathbf{k}) = \begin{pmatrix} H_{11}(\mathbf{k}) & H_{12}(\mathbf{k}) \\ H_{21}(\mathbf{k}) & H_{22}(\mathbf{k}) \end{pmatrix}, \quad (\text{S1})$$

where $H_{11}(\mathbf{k}) = H_{22}(\mathbf{k}) = \epsilon^x + t_1^x \gamma_k + t_2^x \alpha_k + t_3^x \delta_k$ and $H_{12}(\mathbf{k}) = H_{21}(\mathbf{k}) = t_\perp^x + t_{\perp 1}^x \gamma_k + t_{\perp 2}^x \alpha_k + t_{\perp 3}^x \delta_k$ with $\gamma_k = 2(\cos k_x +$

$\cos k_y)$, $\alpha_k = 4 \cos k_x \cos k_y$ and $\delta_k = 2(\cos 2k_x + \cos 2k_y)$. The corresponding on-site energies and hopping parameters are given in Table. S1.

THE TIGHT-BINDING MODEL FOR ANDERSON TRANSITION

To investigate the Anderson transition in disordered systems, we employ the bilayer two-orbital model introduced in Ref. [41], which describes the metallic state at $x = 0$. The Hamiltonian, $H_0(\mathbf{k})$, is expressed in the basis $(d_{rk}^x, d_{rk}^z, d_{bk}^x, d_{bk}^z)$ (with the spin index omitted) as:

$$H_{HP}(\mathbf{k}) = \begin{pmatrix} H_l(\mathbf{k}) & H_\perp(\mathbf{k}) \\ H_\perp^\dagger(\mathbf{k}) & H_b(\mathbf{k}) \end{pmatrix}, \quad (\text{S2})$$

where $H_b(\mathbf{k}) = H_l(\mathbf{k})$. Each block is a 2×2 matrix and is defined as follows:

$$H_l(\mathbf{k}) = \begin{pmatrix} T_{\mathbf{k}}^x & V_{\mathbf{k}} \\ V_{\mathbf{k}} & T_{\mathbf{k}}^z \end{pmatrix}, \quad (\text{S3})$$

and

$$H_\perp(\mathbf{k}) = \begin{pmatrix} t_\perp^x & V_{\mathbf{k}}' \\ V_{\mathbf{k}}' & t_\perp^z \end{pmatrix}. \quad (\text{S4})$$

The individual terms are defined as: $T_{\mathbf{k}}^{x/z} = t_1^{x/z} \gamma_k + t_2^{x/z} \alpha_k + \epsilon^{x/z}$, $V_{\mathbf{k}} = t_3^{xz} \beta_k$, $V_{\mathbf{k}}' = t_4^{xz} \beta_k$ with $\gamma_k = 2(\cos k_x + \cos k_y)$, $\alpha_k = 4 \cos k_x \cos k_y$, $\beta_k = 2(\cos k_x - \cos k_y)$. All parameters used in these expressions are summarized in the upper panel of Table S2. To study the Anderson transition, we also consider a tight-binding model, H_{Mott} , in the same basis to describe the gapped Mott state at $x = 1$. The parameters for H_{Mott} are listed in the lower panel of Table S2. The impurity potential $V_{ij,\alpha\beta} = V_{ij,\alpha\beta}^{Mott}$ is just the difference between H_{Mott} and H_0 .